Quantum Electronics **47** (6) 509 – 521 (2017)

https://doi.org/10.1070/QEL16381

Formation and crystallisation of a liquid jet in a film exposed to a tightly focused laser beam*

S.I. Anisimov, V.V. Zhakhovsky, N.A. Inogamov, S.A. Murzov, V.A. Khokhlov

Abstract. **This paper considers the effect of an ultrashort laser pulse on a thin gold film on a glass substrate at a focal spot size near 1 μm. We analyse the motion and thermal history of a film that has peeled off from the substrate in the heating spot as a consequence of melting. The detached zone is shown to form a dome-shaped bump whose motion is hindered by surface tension. After the dome stops and turns back, towards the substrate, a jet begins to grow on its top. Concurrently, because of the heat dissipation in the film, melt recrystallisation begins, involving first the dome and then the jet. The liquid part of the jet elongates and breaks up into droplets because of the Plateau – Rayleigh instability development. The formation of a neck and the detachment of the last droplet occur in the solidification zone between the crystalline and liquid parts of the jet. The propagation of the crystallisation zone in the jet leads the necking process, so neck disruption occurs in the solid phase under nonequilibrium crystallisation conditions (the melt temperature is hundreds of kelvins lower than the melting point), at limiting mechanical stress and at high deformation rates. As a result, the jet transforms into a high needle with an extremely small tip radius (a few nanometres).**

Keywords: *ultrashort laser exposure, ablation of thin films, single nanostructures.*

1. Introduction

The wide use of lasers for producing surface structures on targets led to the development of a separate subarea of the physics of laser – matter interaction, concerned with surface structuring. This subarea, in turn, comprises a number of research directions, which can be classified according to the morphology and dimensions of surface structures. In this paper, we investigate structures of minimum size, determined by the diffraction limit of optical light focusing. These are compact, rounded structures in the form of a dome or cone [1 – 11] or in the form of a long band on the surface, produced by irradiation through a cylindrical lens [3, 7, 8, 10, 11].

Another direction deals with structures inside large heating spots, tens and hundreds microns in size. Depending on irradiation conditions (laser pulse duration, absorbed energy density, number of laser pulses and laser wavelength), random [12 – 28] or periodic [29 – 34] structures result. Periodic structures are typically produced by a few or multiple shots, as a result of interference between an incident electromagnetic wave and surface plasmons, which are excited as a consequence of the interaction of the incident wave and surface asperities. Random topographies result, first, from the detachment of a runaway layer and/or the top part of a molten and foamed metal and, second, from the freezing of the bottom part of the foam. A model that examines foam formation and breakup and the solidification of the residual foam in the form of random nanostructures was proposed by Zhakhovsky et al. [18, 35].

Interference techniques are used to produce two-dimensional surface arrays of domes isolated from each other, ~1 μm in size and spaced ~1 μm apart [4 – 6]. The formation of nanoparticles is also of research interest, including single particles and particles that are sequentially ejected from separate domes as a result of the breakup of the jet forming in the top of a dome. Also possible is the formation of a cloud of a random set of flying particles in the case of ablation (at a large width of the heating spot) into a gaseous or liquid medium. In addition, there is research interest in the formation of inner structures (cavities and channels) in transparent dielectrics [36].

This paper presents analysis of single structures of minimum size in the form of domes, cones or cones with a sharp tip. Such structures are used in nanoplasmonics [37] and laser printing [1 – 3], as well as to amplify Raman and photoluminescence signals [37]. We are here interested in targets in the form of a thin film on a substrate. Mechanisms of laser-induced film peeling from substrates were first studied by Veiko et al [38, 39]. In what follows, we consider the effect of ultrashort pulses on films whose thickness is smaller than that of the laser heating layer, d_T, in a bulk metallic target [1 – 11, 34, 40].

The article has the following structure: First, we present brief information about processes induced in a thin film by laser irradiation. The following issues are addressed: Section 2.1 – absorbed energy redistribution from the skin layer across the film in a two-temperature stage; Sections 2.2 and

---

[*] Presented at the Fundamentals of Laser Assisted Micro- and Nanotechnologies (FLAMN-2016) International Symposium (Pushkin, Leningrad oblast, 27 June to 1 July 2016).

S.I. Anisimov, N.A. Inogamov, V.A. Khokhlov Landau Institute for Theoretical Physics, Russian Academy of Sciences, prosp. Akad. Semenova 1-A, 142432 Chernogolovka, Moscow region, Russia;
e-mail: office@itp.ac.ru; nailinogamov@gmail.com;
V.V. Zhakhovsky Dukhov All-Russia Research Institute of Automatics, Rosatom, Sushchevskaya ul. 22, Moscow, 127055 Russia;
e-mail: vniia@vniia.ru;
S.A. Murzov Dukhov All-Russian Research Institute of Automatics, Rosatom, Sushchevskaya ul. 22, 127055 Moscow, Russia; Moscow Institute of Physics and Technology (State University), Institutskii per. 9, 141700 Dolgoprudnyi, Moscow region, Russia

Received 24 March 2017
Kvantovaya Elektronika **47** (6) 509 – 521 (2017)
Translated by O.M. Tsarev

2.3 – transition from a fast thermal stage to the dynamics of film detachment (separation) from the substrate; Section 2.4 – spatial distribution of light over the spot, with a maximum in its centre, and dome growth; in Section 2.5, we analyse the capillary deceleration of a dome moving by inertia and jet formation on its top as a result of the deceleration; and Sections 2.6 and 2.7 consider first the crystallisation of the dome and then that of the jet, as well as the competition between the jet crystallisation process and jet breakup into droplets. It is this competition which is responsible for the formation of a high and very sharp needle. The sections following Section 2 address the above issues in greater detail.

2. General picture

2.1. Heating through thermal conduction

Figure 1 shows a film on a substrate. The thickness of the film is d_f and the heating spot radius is R_las. For definiteness, we consider a gold film on glass. We neglect heat conduction in the glass within the heating spot on the timescale $\sim t_\mathrm{s}$, during which the film is in thermal and dynamic contact with the substrate. Here and in what follows, $t_\mathrm{s} = d_\mathrm{f}/c_\mathrm{s}$ (where c_s is the speed of sound in gold).

We consider subpicosecond laser pulses and film thicknesses $d_\mathrm{f} \sim 40-100$ nm. In the wavelength range of interest here, light is absorbed in the metal in a skin layer of thickness $\delta_\mathrm{sk} \sim 10-20$ nm. Thus, the thickness of the film considerably exceeds the skin layer thickness. The absorbed heat begins to be transferred from the skin layer to the film bulk even during the pulse, whose duration is $\tau_\mathrm{las} \sim 10$ fs to 1 ps.

During the time $t_\mathrm{ehc} \sim 1-2$ ps, the electron temperature T_e becomes constant across the film, along the z axis (Fig. 1). At the same time, the temperature T_e remains a function of radius r, $T_\mathrm{e}(r, z, t) \to T_\mathrm{e}(r, t)$ for $t > t_\mathrm{ehc}$, because $R_\mathrm{las} \gg d_\mathrm{f}$. The rapid temperature equalisation in the thickness direction is due to the extremely high values [41] of thermal diffusivity in the two-temperature (2T) stage, χ_2T, where the temperature T_e exceeds the temperature of the ionic subsystem, T_i. The coefficient χ_1T of highly conductive solid and liquid metals (Au, Ag, Cu and Al) is ~ 1 cm^2 s^{-1} under single-temperature (1T) conditions, $T_\mathrm{e} = T_\mathrm{i}$. The temperature equalisation time for a thermally isolated segment of thickness d_f is then $t_\chi = d_\mathrm{f}^2/\chi_\mathrm{1T} \sim 100(d_\mathrm{f}/100)^2$ (where t_χ is in picoseconds and d_f is in nanometres), which is one and half to two orders of magnitude greater than t_ehc.

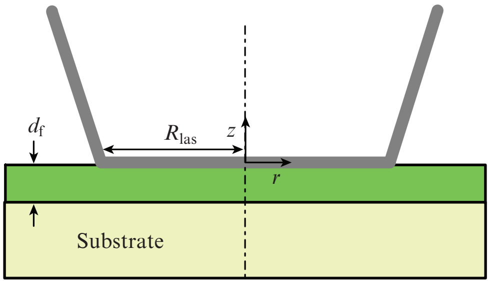

Figure 1. Gold – glass target geometry and the focal spot on the target surface: z and r are cylindrical coordinates. The gold film is located on top of the glass substrate.

In the initial, two-temperature stage, the coefficient χ_2T exceeds χ_1T by the same one and half to two orders of magnitude [41]. The reason for this is that, under 2T conditions, the heat equation splits into two equations [41 – 43]: one for the electronic subsystem and the other for the ionic one. Accordingly, the ratio $\chi_\mathrm{e} = \kappa_\mathrm{e}/c_\mathrm{e}$, which determines the heat propagation rate due to electron heat conduction, includes only electron heat capacity c_e, rather than total heat capacity $c = c_\mathrm{e} + c_\mathrm{i}$, unlike in the 1T case. Note that, at the temperatures under consideration, T_e up to ~ 2 eV and T_i up to ~ 3 kK, electron heat capacity is low compared to total heat capacity: $c_\mathrm{e} \approx (\pi^2/2)k_\mathrm{B}(T_\mathrm{e}/T_\mathrm{F}) \ll c = c_\mathrm{e} + c_\mathrm{i} \approx c_\mathrm{i} \approx 3k_\mathrm{B}$, where k_B is the Boltzmann constant and $k_\mathrm{B}T_\mathrm{F} = E_\mathrm{F}$ is the Fermi energy. According to our density-functional calculations [43], gold has $E_\mathrm{F} \approx 9$ eV. In metals, electron thermal conductivity κ_e prevails, so $\chi_\mathrm{2T} = \chi_\mathrm{e}$. Moreover, electron thermal conductivity κ_e is substantially higher under 2T conditions [43 – 46], because raising T_e from room temperature to ~ 2 eV greatly increases heat capacity c_e, whereas the electron collision frequency, $\nu_\mathrm{e} = \nu_\mathrm{ei} + \nu_\mathrm{ee} \approx \nu_\mathrm{ei}(T_\mathrm{i}) + \nu_\mathrm{ee}(T_\mathrm{e})$, increases less.

2.2. ‘Dividing line’ between the thermal and dynamic stages

Because of the relatively sharp increase in thermal diffusivity χ_2T in the 2T stage, the time taken for film heating throughout its thickness, t_ehc, is short compared to the acoustic timescale $t_\mathrm{s} = d_\mathrm{f}/c_\mathrm{s}$. This is of paramount importance in determining the mechanism underlying detachment of the film from the substrate. The thermal stage proves to lead the hydrodynamic stage. Accordingly, the pressure at the gold – glass interface (Fig. 1) rises sharply long before the rarefaction wave travelling from the boundary with vacuum reaches the contact boundary.

The condition $t_\mathrm{ehc} \ll t_\mathrm{s}$ separates the case of thin films from the case of thick films, which requires a separate analysis. In a bulk target, an ultrashort laser pulse produces a heated layer of thickness d_T over a time of the order of the electron – ion relaxation time t_eq. Thick films are those of thickness $d_\mathrm{f} > d_T$. The films under consideration meet the opposite condition: $d_\mathrm{f} < d_T$. These two cases differ qualitatively from the viewpoint of the nature of the tension of the material in the vicinity of the contact. It should be emphasised that it is this tension which leads to disruption of the contact and peeling of the film. In the case of thin film, the pressure at the film – substrate contact rises almost instantaneously, $t_\mathrm{ehc} \ll t_\mathrm{s}$, and the pressure discontinuity decays in the immobile medium. In the case of thick film, the contact pressure rises later, after a time $\sim t_\mathrm{s}$, and this is related not to the decay of the pressure discontinuity in the immobile medium but to the arrival of a compression wave. In the compression wave, there are both a pressure rise and the motion of particles of the material in the propagation direction of the compression wave.

The thickness of the heated layer is $d_T \sim \sqrt{\chi_\mathrm{2T} t_\mathrm{eq}}$, where t_eq is the temperature equalisation time for T_e and T_i. For example, the d_T of gold is $\sim 100-200$ nm. This is related to the slow ($t_\mathrm{eq} \sim 5-7$ ps) electron – ion relaxation in gold because of the large atomic mass of gold. The defining timescales are the laser pulse duration, $\tau_\mathrm{las} < 1$ ps; the duration of the propagation of an ultrasonic electron thermal wave through the thin film, $t_\mathrm{ehc} \sim d_\mathrm{f}^2/\chi_\mathrm{2T} \sim 1-2$ ps; the electron – ion relaxation time, t_eq; and the hydrodynamic timescale, $t_\mathrm{s} = d_\mathrm{f}/c_\mathrm{s}$.

In the case of gold, there is a marked distinction between the times $t_{\rm ehc}$ (1–2 ps) and $t_{\rm eq}$ (5–7 ps), i.e. the fast thermal wave arrives at the contact before the 2T relaxation reaches completion [7]. This circumstance somewhat complicates the profile of the rarefaction wave travelling from the boundary with vacuum. Moreover, the time variation of the contact pressure $p_{\rm cb}(t)$ also becomes more complex [7]. The point is that the Grüneisen parameters of the electronic ($\mathit{\Gamma}_{\rm e}$) and ionic ($\mathit{\Gamma}_{\rm i}$) subsystems differ significantly: $\mathit{\Gamma}_{\rm e} \sim 1$ [47] and $\mathit{\Gamma}_{\rm i} \sim 2-3$; in gold $\mathit{\Gamma}_{\rm i} \approx 3$. Accordingly, in the case of the thin films under consideration, $\delta_{\rm sk} < d_{\rm f} < d_T$, the motion of the gold surface markedly slows down in the time interval $\tau_{\rm las} < t < t_{\rm ehc}$ because of the drop in electron pressure due to the removal of electronic internal energy from the skin layer. Next, in the time interval $\tau_{\rm ehc} < t < t_{\rm eq} < t_{\rm s}$ the surface slightly accelerates because of the conversion of electron energy into the energy of the ionic subsystem. The former process reduces the specific electron energy and electron pressure on the first characteristic of the rarefaction wave by about a factor of $d_{\rm f}/\delta_{\rm sk}$, to its minimum value, and the latter process raises the total pressure $p = p_{\rm e} + p_{\rm i}$ by about a factor of $\mathit{\Gamma}_{\rm i}/\mathit{\Gamma}_{\rm e}$ relative to its minimum value. The 2T relaxation in copper and aluminium is faster than in gold, $t_{\rm ehc} \sim t_{\rm eq} \sim 1-2$ ps, so there are no such complications. Silver is intermediate in relaxation rate between gold on the one hand and copper and aluminium on the other.

2.3. Hydrodynamics of film peeling

Figure 2 shows pressure forces acting on the gold–glass contact boundary. The glass presses on the film as long as the contact is under positive pressure. Accordingly, the film accumulates the momentum

$$p_z(r,t) = \int_{-\infty}^{t} P_{cb}(r,t')\,{\rm d}t' = \int_{d_{\rm f}} \rho w\,{\rm d}z$$

along the z axis in the direction away from the glass. The integral is here calculated at a fixed radius r along a column running across the film along the z axis; $P_{\rm cb}$ is the pressure at the contact boundary; and w is the z-axis component of the gold film velocity. Before laser exposure, the film was at rest: $p_z(r) \equiv 0$. The centre-of-mass velocity of the column is

$$w_{\rm cm}(r,t) = \frac{p_z(r,t)}{\int_{d_{\rm f}} \rho\,{\rm d}z},$$

where

$$\int_{d_{\rm f}} \rho\,{\rm d}z = \rho_0 d_{\rm f}$$

is the surface density of the film.

The velocity $w_{\rm cm}(r,t)$ increases over time t until the tensile part of the rarefaction wave reaches the contact. The wave propagates in the film, travelling from the boundary between the film and vacuum. Figure 3 demonstrates how pressure profiles vary with time in the stage where two tension waves produce a tensile stress field in the film. One rarefaction wave propagates from the boundary between the film and vacuum, and the other, from the film–glass interface. In our simulations, we used a two-temperature hydrodynamics code. The corresponding system of equations was presented previously [47]. In this code, the laws of conservation of mass and momentum are supplemented by two (rather than one like in the single-temperature analogue) heat balance equations and there are separate energy balance equations for the electronic and ionic subsystems [42, 47]. The thermodynamic equations of state used in our calculations stem from an expression for free energy, which in the case of gold is the sum of the free energies of the ionic and electronic subsystems. The low thermal conductivity of the glass is neglected. In our calculations, the glass is described by a single-temperature equation of state.

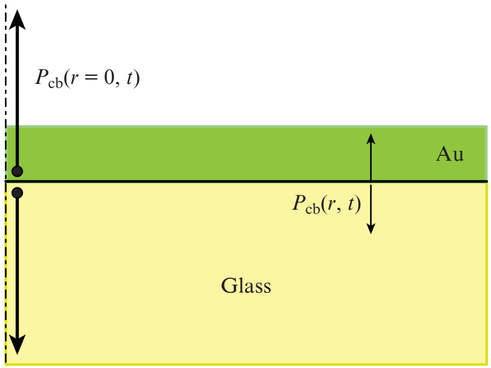

Figure 2. Pressure forces on the film–gold interface. The upward arrows show the directions of the support reaction forces from the glass on a near-contact gold particle when the pressure at the contact boundary (cb) between the gold and glass is positive. This force is maximal on the laser beam axis ($r = 0$).

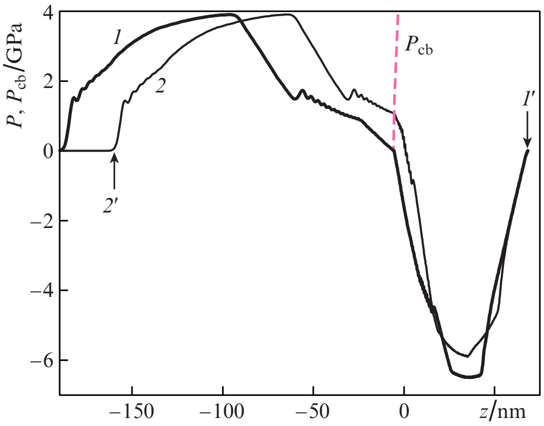

Figure 3. Pressure profiles in the gold film/glass system at time t = (*1*) 30 and (*2*) 35.3 ps. The arrows indicate the position of (*1′*) the boundary of the gold with vacuum and (*2″*) the shock wave in the glass. The gold is located to the right of the $P_{\rm cb}$ line, and the glass, to the left. The shock wave travels much faster than the vacuum boundary.

The parameters used in our simulations: laser pulse duration $\tau_{\rm las} = 0.1$ ps; skin layer thickness $\delta_{\rm sk} = 15$ nm; absorbed fluence $F_{\rm abs} = 40$ mJ cm^{-2}; gold film thickness $d_{\rm f} = 60$ nm; glass substrate. The contact is subject to tension after the pressure at it, $P_{\rm cb}$, drops to below zero. The $P_{\rm cb}(z_{\rm cb})$ curve in Fig. 3 represents the contact pressure as a function of instantaneous contact position $z_{\rm cb}(t)$. It is seen that the pressure $P_{\rm cb}$ drops as the contact shifts towards the glass. The intersections of the $P_{\rm cb}[z_{\rm cb}(t)]$ curve with the $P(z,t)$ pressure profiles at $t = 30$ and 35.3 ps in Fig. 3 indicate the instantaneous position of the contact point in these profiles. Note that the drop in P_{cb} is caused by the combined effect of two rarefaction waves.

An important role is played by the threshold tensile stress that can be withstood by the gold–glass contact (gold adhesion to glass). In what follows, we will restrict our consideration to negligible thresholds. This corresponds to gold and silver films on glass. In this situation, disruption of a contact begins at the instant when the pressure P_{cb} drops to zero. Let P_{cb} become zero at time t_{br}. A rough estimate of t_{br} is related to the acoustic timescale $t_{\mathrm{s}} = d_{\mathrm{f}}/c_{\mathrm{s}}$, which is determined by the time of sound propagation across the film. In the simulation represented in Fig. 3, $t_{\mathrm{br}} = 35.3$ ps and $t_{\mathrm{s}} \approx 20$ ps. Here, t_{br} exceeds t_{s} because of the rarefaction wave broadening in the 2T stage and a slight nonlinearity: in the simulation represented in Fig. 3, the ratio of the maximum pressure to the bulk modulus of gold is $P_{\max}/K = 11/180 = 0.06$.

In the absence of adhesion, the centre-of-mass velocity of the film increases in the time interval $-\infty < t < t_{\mathrm{br}}$ and the contact pressure is positive in this time interval. The velocity of the film after the detachment from the substrate,

$$w_{\mathrm{cm}}^{\mathrm{br}}(r) = w_{\mathrm{cm}}(r, t_{\mathrm{br}}) = (\rho_0 d_{\mathrm{f}})^{-1} \int_{-\infty}^{t_{\mathrm{br}}} P_{\mathrm{cb}}(r, t')\,\mathrm{d}t', \tag{1}$$

is roughly proportional to the local absorbed fluence $F_{\mathrm{abs}}(r)$. Indeed, because of the rapid temperature equalisation across the film, $t_{\mathrm{ehc}} < t_{\mathrm{eq}} < t_{\mathrm{s}}$, the absorbed energy per unit volume is $F_{\mathrm{abs}}/d_{\mathrm{f}}$. The pressure is $P = \Gamma F_{\mathrm{abs}}/d_{\mathrm{f}}$. The velocity of the film after it peeled off is then

$$w_{\mathrm{cm}}^{\mathrm{br}}(r) \approx \frac{Z_{\mathrm{g}}}{Z_{\mathrm{Au}}} \frac{\Gamma F_{\mathrm{abs}}}{Z_{\mathrm{Au}} d_{\mathrm{f}}}.$$

In deriving this estimate, we used relation (1), assumed that $t_{\mathrm{br}} \approx t_{\mathrm{s}}$ and took into account the pressure drop upon the decay of the pressure discontinuity across the contact of two half-spaces with acoustic impedances Z_{g} (substrate–glass) and Z_{Au} (film–gold). Numerical calculations (see the example in Fig. 3) yield the approximate relation

$$w_{\mathrm{cm}}^{\mathrm{br}}(r) \approx \frac{60 F_{\mathrm{abs}}(r)/40}{d_{\mathrm{f}}/100}, \tag{2}$$

where $w_{\mathrm{cm}}^{\mathrm{br}}$ is in metres per second; F_{abs}, in mJ cm^{-2}; and d_{f}, in nanometres. Formula (2) is valid in the case of thin films, $d_{\mathrm{f}} < d_T$, where d_T is the thickness of the layer heated in the 2T stage. For gold, the heated layer thickness is 100–200 nm. The lateral redistribution of the absorbed heat in a time interval near $t_{\mathrm{br}} \sim t_{\mathrm{s}}$ is insignificant for $R_{\mathrm{las}} \gg d_T$, where R_{las} is the spot radius (see Fig. 1). Thus, the radial energy distribution, $F_{\mathrm{abs}}(r)$, roughly reproduces the radial distribution of the incident energy, $F_{\mathrm{inc}}(r)$. In the intensity range of interest here, the increase in absorption coefficient towards the centre because of the increase in intensity towards the centre is relatively small.

2.4. Laser beam with an intensity maximum on its axis and dome formation

The intensity distribution over the heating spot on a film being illuminated can be controlled by optical means. Since according to (2) the detachment rate is proportional to the local fluence, the shape of a flying film can be controlled by varying the intensity distribution over the spot. We are interested in the smallest, diffraction-limited spots. In such a situation, the intensity is usually highest in the centre of the spot. The absorbed fluence distribution can be approximated, for example, by a Gaussian, $F_{\mathrm{abs}}(r) = F_{\mathrm{c}} \exp(-r^2/R_{\mathrm{las}}^2)$. While flying, the part of the film detached from the substrate takes the shape of dome:

$$z(r,t) = w_{\mathrm{cm}}^{\mathrm{br}}(r)\,t, \quad w_{\mathrm{cm}}^{\mathrm{br}}(r) = w_{\mathrm{c}}\left[\exp\left(-\frac{r^2}{R_{\mathrm{las}}^2}\right) - \Delta\right], \tag{3}$$

where w_{c} is the velocity in the centre and $\Delta \ll 1$ if there is weak film adhesion to the glass. Time t is measured from the instant when an ultrashort pulse reaches the target. This is because Eqn (3) for $z(r,t)$ is applied at a considerable film–substrate separation, $z \sim R_{\mathrm{las}}$, so that the velocity $w_{\mathrm{cm}}^{\mathrm{br}}$ is several tens of metres per second. The time needed to pass a distance $z \sim 1$ μm at such velocity is tens of nanoseconds. On a timescale of ~1 ns, the variations in reference time t related to the pulse duration (less than 1 ps) and acoustic time (~10 ps) are insignificant. Note that at shifts $z \sim R_{\mathrm{las}} \gg d_{\mathrm{f}}$, the thickness of the dome shell is small compared to the height z of the shell.

According to (3), flight by inertia will continue until surface tension and crystallisation will become significant. These issues are addressed quantitatively in Section 3. Qualitative considerations necessary for general understanding are presented in the next two subsections.

2.5. Capillary deceleration of a dome and jet formation

In the initial stage, when the effects of surface tension and solidification are still weak, the shape of the dome follows the backpressure distribution (Fig. 2) and the intensity distribution across the focal spot [see (3)]. Let us take into account capillarity. Figure 4 shows the shape of the film (in the shape of a dome) detached from the substrate. According to Eqn (3), if surface tension is neglected this shape corresponds to the velocity distribution $w_{\mathrm{cm}}^{\mathrm{br}}(r)$. Component $\boldsymbol{N}$ of the surface tension force (vector $\boldsymbol{C}$ in Fig. 4) acts in the direction of deceleration and reversal of the normal velocity component $w_{\mathrm{cm}}^{\mathrm{br}}(r)$. Thus, capillarity changes the shape of the dome.

The capillary force $\boldsymbol{C}$ in Fig. 4 makes an angle with the S axis. Because of this, in addition to the normal component $\boldsymbol{N}$ there is an $\boldsymbol{A}$ component, directed to the axis of the dome. It is this component that leads to the displacement of the dome shell material towards the axis. As a result of the motion of liquid particles towards the axis, which reach it in a finite

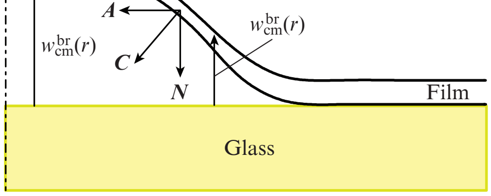

Figure 4. Dome-shaped elevation of a film produced by the velocity field (3); S is the symmetry axis of the axisymmetric dome, $\boldsymbol{C}$ is the surface tension force, $\boldsymbol{N}$ is the normal component of force $\boldsymbol{C}$, and $\boldsymbol{A}$ is the force component directed to the dome axis.

time, the material accumulates near the axis. Note a distinction between 2D and 3D cases. In planar geometry (where a planar x, y coordinate system should be used instead of the cylindrical r, z coordinate system), accumulation of a material leads to the formation of a 2D droplet. The droplet may turn back (i.e. towards the substrate) under the action of surface tension [10, 48]. Such droplets form debris on the surface. The formation of debris from frozen droplets on the substrate surface was observed previously in 2D [49] and 3D [34, 40, 49] experiments. In the 2D case, no outgoing jet is formed, because an insufficient amount of the material accumulates in the centre [10, 48]. In axisymmetric 3D geometry, radial flows of the material converge to the dome axis. Accordingly, a much larger amount of the material accumulates near the axis in comparison with the 2D case. In such a situation, the material arriving in radial direction begins to outflow from the accumulation zone along the axis, mostly upwards, away from the substrate. But also possible is the formation of a reverse jet, directed towards the substrate [7]. A reverse jet was observed in experiments [2, 5, 50].

Jet formation can be thought of as a manifestation of Rayleigh–Taylor instability. Indeed, acceleration is directed from a low-density medium (vacuum or a gas outside the dome in Fig. 4) to a denser medium (the material of the dome shell). One analogue of such instability is instability of hydrostatic equilibrium of a horizontal flat layer in the vertical gravity field, where the weight of the layer is compensated for by the pressure difference of a low-density gas above and below the layer.

Paradoxically, deceleration is due to surface tension forces, even though capillarity is simultaneously a stabilising factor. Sometimes, Plateau–Rayleigh instability of a liquid cylinder is thought of in such a paradoxical manner (as a version of Rayleigh–Taylor instability).

2.6. Crystallisation

As mentioned in Sections 2.1 and 2.2, a laser shock leads to rapid heating. At a sufficiently high absorbed energy $F_{\rm abs}$, the film in the heating spot melts, then slowly cools and solidifies. The power of the absorbed energy ($F_{\rm abs}$) loss through radiative cooling is low. Cooling is determined mainly by heat conduction, with heat spreading over the metallic film to the cold peripheral part of the film (if heat transport in the substrate is neglected: Fig. 5a, red arrow), or spreading over the film in Fig. 5c, with heat transfer to the substrate behind the film detachment spot (Figs 4, 5). In axisymmetric geometry, the heat flow being removed spreads radially, so beyond the heating spot the temperature rapidly decreases to its initial level, 300 K, in infinity. The black arrows in Fig. 5 demonstrate how the crystallisation zone propagates from the periphery of the spot to its centre. After the solidification of the liquid phase in the central part, the entire solid phase cools to its initial temperature.

There is a competition between inertia–capillary dynamics and crystallisation. On the one hand, motion is a combination of inertial motion (flight of the material of the film by inertia after detachment from the substrate) and effects related to surface tension (for this reason, we deal here with inertia–capillary dynamics; see Section 2.5). On the other hand, crystallisation greatly reduces the stretchability of the film and the possibility of mechanically bending it. After freezing, motion ceases and gives way to decaying elastoplastic oscillations of the solidified film.

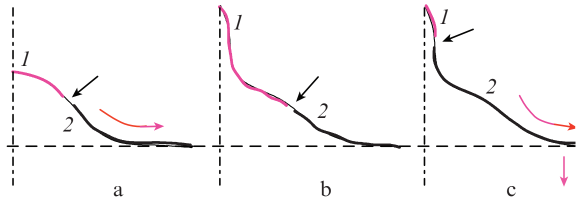

Figure 5. (Colour online) Solidification of a liquid zone in the film due to cooling of the liquid in the cases of (a) a dome and (b, c) a dome plus a jet on its tip. Crystallisation sharply restricts the mechanical mobility of the dome shell. The black arrows in panels b and c show the propagation of the recrystallisation zone: (*1*) liquid phase, (*2*) solid phase. The red arrows in panels (a) and (c) represent heat flows. In panel (a), heat transfer to the substrate can be neglected. In panel (c), heat dissipation through the film is accompanied by heat removal to the substrate.

In this competition, either the capillary complication of the dome shape or the termination of this complication as a result of the solidification of the material prevails, depending on the ratio of the capillary number w_σ to the thermal number w_χ, which characterises the cooling rate. The capillary number is $w_\sigma = v_\sigma / w^{\rm br}_{\rm cm}(r=0)$ and the thermal number is $w_\chi = v_\chi / w^{\rm br}_{\rm cm}(r=0)$, where $w^{\rm br}_{\rm cm}(r=0)$ is the velocity of the film after detachment in the centre of the laser spot; $v_\sigma = 2\sqrt{\sigma/(\rho d_{\rm f})}$ is the capillary velocity scale; σ is the surface tension coefficient of the melt; $\rho d_{\rm f}$ is the initial density of the film per unit area; $v_\chi = \chi / R_{\rm las}$ is the cooling rate of the heating spot; $\chi = \kappa / c$ is thermal diffusivity; κ is the thermal conductivity of the film material under 1T conditions; $c = c_{\rm e} + c_{\rm i} \approx 3k_{\rm B}n_0$ is total heat capacity; and n_0 is the atomic concentration.

At a high cooling rate, when $w_\chi \gg w_\sigma$, the flying dome solidifies before the reversal point of the film material (rapid freezing regime, Fig. 6a). In such a situation, no jet is formed, because jet formation begins after the dome stops and turns back. Note that jet formation requires as well the dome height H at the reversal point be roughly equal to the spot radius $R_{\rm las}$ (Fig. 6). In the case of strong surface tension or a low rate of detachment from the substrate, $w^{\rm br}_{\rm cm}(0) \ll v_\sigma$, we have $H \ll R_{\rm las}$ at the reversal point and jet formation is impossible.

Electron-microscopic examination (a long time after laser exposure) under rapid freezing conditions shows a

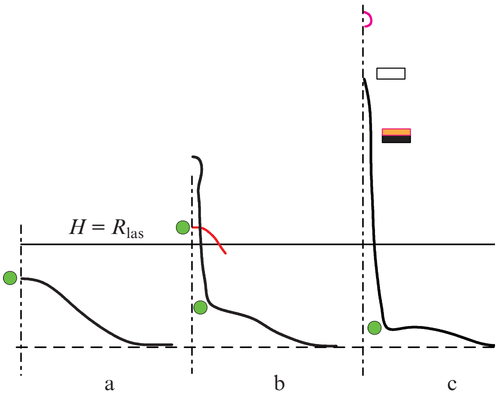

Figure 6. Sequence of events, boundaries between different stages and final morphology of a forming dome with a jet. The shape of the solidified dome is determined by the relationship between the velocities $w^{\rm br}_{\rm cm}(0)$, v_σ and v_χ (see Sections 2.6, 2.7 and 3).

rounded or conical dome with no solidified jet on its tip (Fig. 6a). To put it more precisely, there are characteristic hydrodynamic ($t_{\rm hd} = R_{\rm las}/w^{\rm br}_{\rm cm}(0)$), capillary ($t_\sigma = R_{\rm las}/v_\sigma$) and crystallisation ($t_\chi = R_{\rm las}/v_\chi$) times. As mentioned above, capillarity has no time to show up if $t_\chi \ll t_\sigma$, i.e. if, because of the crystallisation, the upward motion of the dome has no time to stop. It should be emphasised that it is after such motion stops that jet formation and growth begin. For the formation of a frozen dome, the freezing time t_χ should not exceed the hydrodynamic time $t_{\rm hd}$. In the opposite limit, $t_\chi \gg t_\sigma$, no dome is formed. In the case of a thin ($d_{\rm f} < d_T$) film (see Section 2.2), in place of a heating spot there remains a hole with a beaded rim, because the central part of the dome breaks up before solidifying. Only the bead on the edge of the shell recrystallises and thus persists for a longer time. The reason for this is that the radial extension of the bead is small compared to $R_{\rm las}$ and, hence, its cooling time is shorter than the time t_χ evaluated from the spot radius $R_{\rm las}$.

There are complex situations in which surface tension and crystallisation should be taken into account together with jet and dome breakup processes. Let us consider them.

2.7. Capillarity and crystallisation

Figure 6 compares inertia–capillary hydrodynamics and crystallisation in the case of jet breakup. The simplest regime is fast freezing (Fig. 6a), where $t_\chi < \sim t_{\rm hd}$ or, if the condition $t_\sigma < t_{\rm hd}$ is satisfied, $t_\chi < t_\sigma$. In this regime, considered in Section 2.6, the coordinate of the top of the dome, $H(t)$, first increases monotonically, which is followed by saturation after a time $\sim t_\sigma$. As a result, the function $H(t)$ reaches a maximum, $H_{\rm max}$, marked by a circle in Fig. 6a. Note that $H_{\rm max} < R_{\rm las}$ in the fast freezing regime. The dome has a parabolic shape for $H_{\rm max} \ll R_{\rm las}$ and becomes conical for $H_{\rm max} \sim R_{\rm las}$.

At reduced surface tension, with $t_\sigma \gtrsim t_{\rm hd}$ and $t_\chi > t_\sigma$, the dome morphology is complicated by jet formation on the top of the dome. As mentioned above, a jet is formed after the point $H_{\rm max}$, also referred to here as the reversal point, is reached. Together with this event, the trajectory splits into a $z_{\rm high}$ trajectory of the highest point (the top of the jet) and a $z_{\rm low}$ trajectory of the dome (Fig. 7). The maximum ($t_{\rm max}$, $H_{\rm max}$) and splitting are illustrated in Fig. 7 by the example of molecular dynamics (MD) simulation no. 203, with a long freezing time. Because of this, solidification did not impede inertia–capillary hydrodynamics. Without solidification, surface tension acts constantly. This leads to a large decrease in dome height $H(t)$. It is worth repeating that for jet formation the maximum should be of the order of or greater than the spot radius $R_{\rm las}$.

Figure 8 illustrates the evolution of the dome at a relatively weak capillarity (like in Fig. 7) but a considerable freezing rate (in contrast to Fig. 7): $t_\sigma/t_{\rm hd} = 1/w_\sigma = 2.6$, $t_\sigma = 440$ ps, $w_\sigma = 0.39$, $w_\chi = 0.34$ and $t_\chi = 490$ ps (MD simulation no. 220). Like in Fig. 7, it is seen in Fig. 8 that the dome rises, reaching the maximum height $H_{\rm max}$ at $t_{\rm max}$, then generates a jet and begins to subside. Number 1 in Fig. 8 refers to the reversal point, analogous to the maximum $H_{\rm max}$ at $t_{\rm max}$ in the $z_{\rm low}$ curve in Fig. 7. In Fig. 8, $H_{\rm max} = 1.24R_{\rm las}$. The maximum is reached at $t_{\rm max} = 290$ ps ($t_{\rm hd} = 170$ ps), with $t_{\rm max}/t_\sigma = 0.7$. It is seen that, despite the fivefold difference in length and time scales ($R_{\rm las}$ is 300 nm in Fig. 7 and 65 nm in Fig. 8; $t_\sigma = 2.6$ and 0.44 ns, respectively) and the marked difference in freezing rate, $t_{\rm max}$ and $H_{\rm max}$ in Fig. 7 (presented in dimensionless coordinates) are very similar to those in Fig. 8 (0.7 and 1.24). Clearly, this is due to the equal values of the capillary parameter w_σ and rather slow freezing. Thus, the dynamics of the process are scaled with good accuracy using the parameters w_σ and w_χ. This allows a situation with much large dimensions of structures (with $R_{\rm las}$ of several and, possibly, tens of microns) to be simulated using relatively small MD systems.

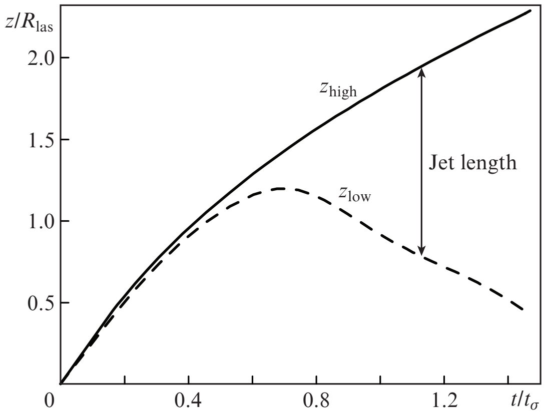

Figure 7. Example of simulation at a relatively weak surface tension and very slow freezing: $t_\sigma/t_{\rm hd} = 1/w_\sigma = 2.6$, $t_\sigma = 2.6$ ns and $t_\sigma \ll t_\chi$. The upper and lower curves refer to the instantaneous position of the highest point of the structure, $z_{\rm high}$, and the top point of the dome, $z_{\rm low}$. Before the reversal point of the dome, $t_{\rm max}$ (the maximum in the $z_{\rm low}$ curve), $z_{\rm high} \approx z_{\rm low}$. At the reversal point, the formation of a jet of length $z_{\rm high} - z_{\rm low}$ begins. After the reversal point, the dome below the jet begins to subside under the action of surface tension [two circles in Fig. 6b: the upper circle refers to the reversal point, with the film molten (grey curve), and the lower circle in Fig. 6b shows the position of the subsided and solidified dome].

One can see a narrow transition zone between the shell of the hollow dome and the jet (the lower circles in Figs 6b and 6c and point 3 in Fig. 8). Surprisingly, there is no density wave propagating through the liquid film from the jet to the dome.

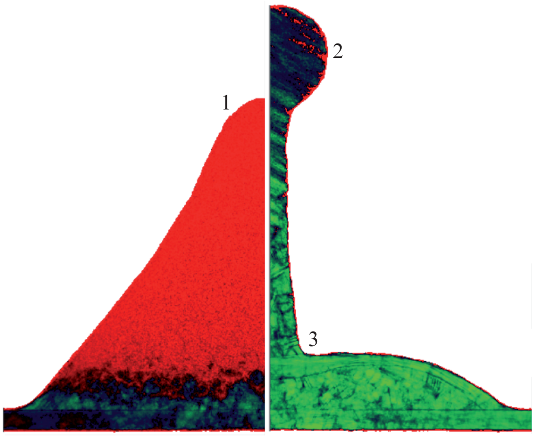

Figure 8. (Colour online) The dome reaches the maximum height in a liquid state (point 1) and then begins to sink and crystallises. After solidification, the height of the dome (point 3) is small. The downward motion of the dome is accompanied by the formation of a jet, whose height in the solid state is shown by point 2 (cf. with the $z_{\rm low}$ and $z_{\rm high}$ curves in Fig. 7).

The dome turns back at point 1 and moves downwards under the action of capillary forces, even though there is a massive jet in its centre. This downward motion stops at point 3 only after freezing.

Inogamov et al. [7] developed a simple linear theory valid at small deviations of the dome from the plane of the substrate. At high values of the parameter w_σ (and without freezing, $w_\chi = 0$), the theory describes all the hydrodynamic history of the inertia–capillary motion of the film that has peeled off: from upward motion and the arrest stage to downward motion to the point of collision with the substrate. This is not surprising. What is surprising is that nonlinear dynamics with $w_\sigma \sim 1$ and a heavy near-axis jet maintain a downward moving dome (as in the linear case), which is described by the right-hand branch of the function $z_{\rm low}$ in Fig. 7.

Therefore, the near-axis jet exists as a 'black hole' absorbing the mass flow directed to the axis (see Section 2.5 and Fig. 4). This is a nonradiative 'hole' emitting no disturbances through the thin film, which adjoins vacuum on both sides. Such interpretation is suggested by comparison of MD simulation results and calculations of dome dynamics with equations of thin shell derived previously [7]. Both MD simulation and the equations of thin shell give almost identical descending branches of the $z_{\rm low}$ function in Fig. 7. In the problem with a thin shell, a jet is formed because of the self-intersection of the shell contour [7]. In the calculation represented in Fig. 7, the mass of the jet rises almost linearly, starting from the jet formation at $t \approx 0.6t_\sigma$ and until $t \approx 2t_\sigma$, when the descending dome is very close to the plane of the substrate. In this process, the mass rises from zero to 60% of the entire mass involved in motion in a circle of radius $R_{\rm las}$. This result agrees with experimental estimates of the mass detached in the form of a droplet or droplets [5, 49].

Figure 9 illustrates the effect of cooling rate on inertia–capillary dynamics. The left-hand side corresponds to MD simulation no. 223, with the same detachment rate $w_{\rm cm}^{\rm br}(0)$ and capillary velocity v_σ as in the calculation represented in Fig. 8 and on the right of Fig. 9. But the cooling rate on the left of Fig. 9 is twice higher: w_χ is 0.68 rather than 0.34, in contrast to Fig. 8. Accordingly, the path made by the dome on the left of Fig. 9 from the arrest to the plane of the substrate is smaller than that on the right-hand side (cf. the freezing points 3 and 3′). In both simulations the reversal point is reached at the same instant in time (about 300 ps). The left-hand side of Fig. 9 corresponds to t = 1.2 ns, and the right-hand side, to 2.7 ns.

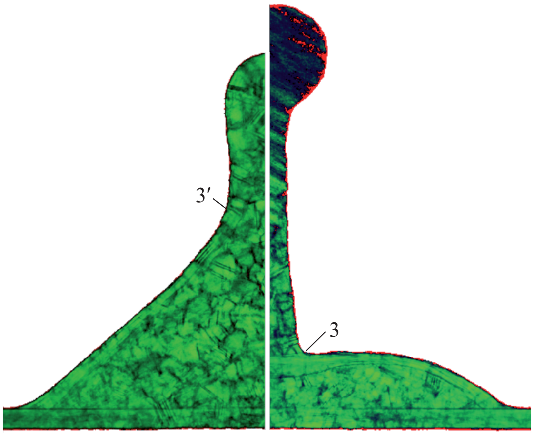

Figure 9. (Colour online) Effect of crystallisation rate on the formation of the final morphology of the forming dome. The cooling rate on the left side is twice higher, so the left side freezes faster and point 3′ (the beginning of the shoulder between the jet and dome) is located higher than point 3.

Figure 10 shows the inner structure of the frozen hollow cone presented in Fig. 9. Note a considerable decrease (by about a factor of 3) in the thickness of its shell relative to its initial thickness. To the initial thickness corresponds the height of the pedestal on the left of Fig. 9 and the thickness of the film on its right-hand side. The glass substrate is under the pedestal. It is also worth noting the narrow inner pit in the head part of the dome under the forming jet.

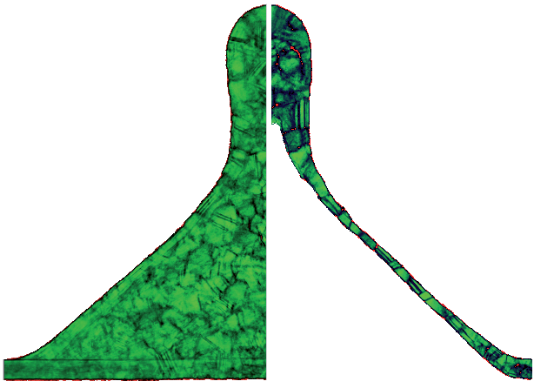

Figure 10. (Colour online) Section of the conical dome shown on the left of Fig. 9. One can see a conical shell and the germ of a jet near the top of the cone.

2.8. Capillarity, crystallisation and breakup of the jet

Figures 6a and 6b, which were analysed above, corresponded to hydrodynamic motion of the film material away from the substrate and along it. There was no thermomechanical ablation (detachment and removal of the material from the substrate). Owing to mechanical bonding along the film, the forming dome is still rather well adherent to the substrate. Thermomechanical ablation of bulk targets, where detachment is brought about by overcoming the cohesion of a condensed medium, is known to differ qualitatively from evaporative ablation. How does thermomechanical ablation (i.e. complete detachment of the film material from the substrate) occur in the case of thin-film targets? Clearly, complete detachment of part of the film material from the film involves an increase in its height over the substrate to the point of disintegration of the film. A transition to ablation is caused by the increase in detachment rate $w_{\rm cm}^{\rm br}$ with increasing absorbed fluence $F_{\rm abs}$.

Thus, there are thresholds for detachment in terms of fluence $F_{\rm abs}$ and detachment rate $w_{\rm cm}^{\rm br}$. The question of freezing will be addressed below. Two scenarios are possible, depending on w_σ. In one of them, w_σ is extremely low, e.g. $w_\sigma = 0$. The shape of a dome flying by inertia then reproduces the intensity distribution over the spot, given by Eqn (3). Clearly, flight by inertia, without surface tension or freezing, cannot be stopped. Eventually, the entire dome will break up into fragments flying away, without bonding with the film beyond the detachment spot. The other scenario takes place at finite

w_σ values. Here, during motion, self-intersection of the film begins and a jet forms. The rest of the dome beyond the jet returns to the substrate, and most of the jet breaks up into droplets, which fly away (ablation) by virtue of Plateau–Rayleigh instability (PRI). Slightly above threshold, one droplet separates and flies away. This process is illustrated in Fig. 6c (the semicircle in the top part represents a molten droplet). Consider the latter scenario taking into account freezing, i.e. at finite values of the thermal parameter w_χ. This is the subject of Section 3.

3. Tip formation

3.1. Plateau–Rayleigh instability

Figure 6c corresponds to the process involving a strong capillary effect, ablation (jet breakup) and freezing. Below the detachment threshold, the droplet persists on the top of the jet, as in Figs 6b, 8 and 9 (at the right). Above this threshold, jet breakup begins. The larger the excess over threshold, the larger the number of detaching droplets. Dropelts detach because of the development of PRI in the liquid part of the jet. In the case of multiple jet breakup into droplets, the process is more complex. The first droplet is the largest, the fastest and the hottest in the sequence of droplets.

Accelerated development of PRI requires a substantial decrease in jet diameter on account of its longitudinal stretching due to the velocity gradient along the length of the jet, $\partial w/\partial z$. The inverse of the maximum increment, $1/\gamma_{\max} \approx 3\sqrt{\rho R_{\mathrm{j}}^3/\sigma}$, characterises the PRI development time in the case of a circular cylinder with an immobile liquid. Here, R_{j} is the diameter of the cylinder. The corresponding characteristic velocity is $v_{\mathrm{PR}} = R_{\mathrm{j}}\gamma_{\max} \approx 0.3 v_\sigma \sqrt{d_{\mathrm{f}}/R_{\mathrm{j}}}$, where $v_\sigma = 2\sqrt{\sigma/(\rho d_{\mathrm{f}})}$. Typically, $d_{\mathrm{f}} \sim (2\%–5\%)R_{\mathrm{las}}$ and $R_{\mathrm{j}} \sim 7\% R_{\mathrm{las}}$. For PRI development, v_{PR} should exceed the elongation rate $(\partial w/\partial z)\lambda_{\max}$ of a liquid cylinder of the order of the wavelength $\lambda_{\max} \approx 9R_{\mathrm{j}}$ in length, which corresponds to the most stable mode in the case of PRI. In the study of instability, the elongation rate can then be neglected and we can return to the immobile liquid approximation.

The longitudinal jet velocity (w) distribution is approximately a linear function of z. The jet has a maximum velocity in the vicinity of the neck of the top (head) droplet of the jet. The droplet size gradually increases because the neck moves along the jet, spanning new and new portions of the material. Inside the droplet, the instantaneous velocity $w_{\mathrm{head.drop}}(t)$ is spatially uniform. The value of $w_{\mathrm{head.drop}}(t)$ decreases slowly because new portions of the material have smaller z-components of their momentum.

The velocity at which the material of the jet enters the head droplet is $\Delta v_{\mathrm{j}} = v_\sigma|_{R_{\mathrm{j}}}/\sqrt{2} = \sqrt{2\sigma/(\rho R_{\mathrm{j}})}$, where $v_\sigma|_{R_{\mathrm{j}}} = 2\sqrt{\sigma/(\rho R_{\mathrm{j}})}$. This follows from the law of conservation of momentum. Consider an immobile liquid cylinder with a head droplet that moves with velocity Δv_{j} relative to the cylinder. The conservation of momentum means that $\sigma 2\pi R_{\mathrm{j}} t = \rho\pi R_{\mathrm{j}}^2 l \Delta v_{\mathrm{j}}$ (where t is the time during which the droplet moved and l is the distance that the droplet passed along the cylinder). Then we have $l/t = \Delta v_{\mathrm{j}}$. From here we obtain the above formula for Δv_{j}.

From the law of conservation of energy, $\sigma 2\pi R_{\mathrm{j}} l = \rho\pi \times R_{\mathrm{j}}^2 l \Delta v_{\mathrm{j}}^2/2 + Ql$, we find that half of the work done by capillary forces, $\sigma 2\pi R_{\mathrm{j}} l$, goes into the kinetic energy of the droplet and half dissipates into heat (Q characterises dissipation due to friction). The ratio of the surface area of the droplet to its volume is small compared to that of the cylinder. The radius of the cylinder that has the droplet on its top is taken to be small compared to the droplet radius. Because of this, we neglect the capillary energy of the droplet in the law of conservation of energy. An analogous relation for a peripheral cylindrical droplet at the edge of a flat film was derived previously [7]. A ‘droplet’ is cylindrical when it is located on the linear edge of the half-plane formed by the film with a lateral boundary. Due to friction, the droplet heats up by $\Delta T = (\rho \Delta v_{\mathrm{j}}^2/2)/c = \sigma/(2k_{\mathrm{B}} n R_{\mathrm{j}})$, where $c \approx 2k_{\mathrm{B}} n$ is the heat capacity of the melt per unit volume and $n \approx 6 \times 10^{22}$ cm^{-3} is the atomic concentration. Substituting $\sigma \approx 1000$ dyn cm^{-1}, $R_{\mathrm{j}} = 0.05 R_{\mathrm{las}}$ and $R_{\mathrm{las}} = 1$ μm, we obtain small heating: $\Delta T = 12$ K.

Let us estimate the jet length at which the above-mentioned condition $v_{\mathrm{PR}} > (\partial w/\partial z)\lambda_{\max} = 9(\partial w/\partial z)R_{\mathrm{j}}$ begins to be fulfilled. It follows from analysis of calculation results that $\partial w/\partial z \sim 0.5 w_{\mathrm{cm}}^{\mathrm{br}}(0)/l_{\mathrm{j}}$, where $0.5 w_{\mathrm{cm}}^{\mathrm{br}}(0)$ is the jet velocity immediately before the neck of the head droplet and l_{j} is the variable jet length. The estimate is valid at $l_{\mathrm{j}} \sim R_{\mathrm{las}}$. Comparing velocities, we find that, for jet breakup into droplets by the PRI mechanism, the jet length should reach $\sim 11 w_{\mathrm{cm}}^{\mathrm{br}}(0) R_{\mathrm{j}}^{3/2} \times \sqrt{\rho/\sigma}$. Substituting $\sigma \approx 1000$ dyn cm^{-1}, $R_{\mathrm{j}} = 0.05 R_{\mathrm{las}}$, $R_{\mathrm{las}} = 1$ μm and $w_{\mathrm{cm}}^{\mathrm{br}}(0) = 50$ m s^{-1}, we find that the jet length should be ~ 1 μm. Then, with allowance for the height of the reversal point, the distance to the plane of the substrate will be $\sim 2R_{\mathrm{las}}$. At the same time, it follows from MD simulations that the jet length at the instant of disruption is considerably greater (by a factor of 1.7 to 3). The likely reason for this is that the rate of PRI development to complete jet breakup is markedly slower than $v_{\mathrm{PR}} = R_{\mathrm{j}}\gamma_{\max}$. Unger et al. [2] experimentally observed the flight of detached droplets.

Typical MD simulations give $t_1 = (4 \pm 0.5)t_\sigma$ and $h_1 = (3.5–5)R_{\mathrm{las}}$ for the instant and position of the first disruption of the jet. Here $t_\sigma = R_{\mathrm{las}}/v_\sigma$; $v_\sigma = 2\sqrt{\sigma/(\rho d_{\mathrm{f}})}$; and h_1 is the distance from the point of the first disruption to the plane of the substrate. The values of t_1 and h_1 are given for a moderate excess over the threshold for the detachment of a single droplet from the jet. Under such conditions, the parameter $1/w_\sigma$ is about twice this threshold. Near the threshold, the coefficient ζ in the formula for the jet velocity, $\zeta w_{\mathrm{cm}}^{\mathrm{br}}(0)$, tends to zero. At a moderate excess, we have $\zeta \sim 0.5$. At a large excess over threshold, not only the jet but also the top part of the dome break up. The parameter $1/w_\sigma$ then increases by about four times in comparison with threshold and the coefficient ζ increases to unity. That the coefficient ζ is less than unity means that part of the initial velocity $w_{\mathrm{cm}}^{\mathrm{br}}(0)$ is lost upon the formation of a dome because of the capillary deceleration.

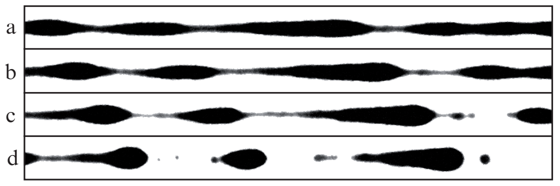

Figure 11. Multiple jet breakup at times $t_1 \sim (4–7)t_\sigma$. Simulation no. 221 at times (a) 3.77, (b) 3.94, (c) 4.1 and (d) 4.26 in units of t_σ. The left and right boundaries of the frames, at $6.6R_{\mathrm{las}}$ and $11.3R_{\mathrm{las}}$, respectively, are measured from the plane of the substrate. The first disruption in simulation is located at a height $h_1 = 3.5R_{\mathrm{las}}$. Calculation parameters: $w_\sigma = 0.19$ and $w_\chi = 0.17$. All of the material is here in a molten state.

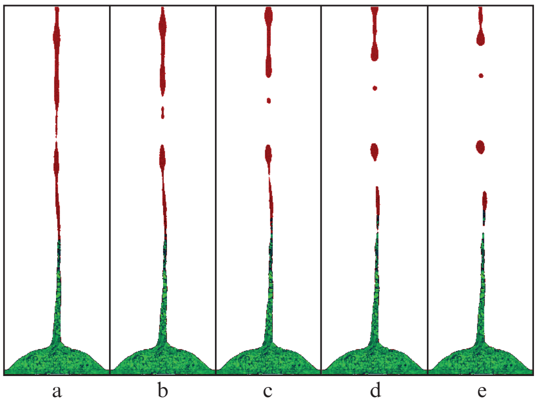

Figure 12. (Colour online) Formation of lower droplets in a sequence of droplets that a jet breaks up into. Calculation parameters: $w_\sigma = 0.19$ and $w_\chi = 0.345$; simulation no. 225; pedestal length, 140 nm. Times of (a) 4.43, (b) 4.59, (c) 4.76, (d) 4.92 and (e) 5.08 in units of t_σ. After the lowermost disruption, which ends in a solid state, the frozen jet transforms into a rod with a sharp tip. The melt is shown red and the crystalline phase is shown green.

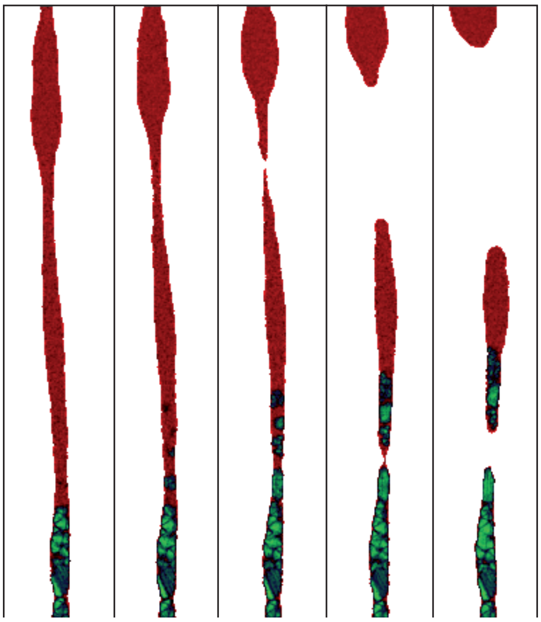

Figure 13. (Colour online) Regions near the lowermost disruption of the jet, cut from the simulation in Fig. 12. The homogeneous crystallisation zone has time to propagate upwards, to above the narrowing neck, before disruption, which changes its character in the final stage. The formation of a frozen droplet on the top of the rod is then ruled out. The formation of such a droplet drastically reduces the sharpness of the nanotip.

At a moderate excess over threshold, the jet breaks up into many droplets soon after the first disruption. In the case of such breakup, droplets are formed above the first disruption (Fig. 11). Moreover, one or two additional disruptions may occur below the first disruption (Figs 12, 13). The calculations represented in Figs 11 and 12 differ in cooling rate: in Fig. 11, the cooling rate is a factor of 2 lower. Accordingly, surface tension has a longer lasting decelerating effect and the jet velocity is somewhat lower at equal surface tension coefficients and initial velocities $w_{\rm cm}^{\rm br}(0)$.

3.2. Interaction of a decaying jet with the crystallisation zone

In Section 3.1, we considered the breakup of the liquid part of a jet. The decaying part is located above the open rectangle in Fig. 6c. Below it there is a mark consisting of a red and a black rectangle. At a given instant of time, the crystallisation zone is located in this region. The melt in the upper part of the jet is shown red and the solid phase, i.e. the solidified region in the lower part of the jet, is shown black. The crystallisation zone shifts upwards over time, thus approaching the droplet detachment zone. The MD simulation results presented in Figs 12 and 13 demonstrate how the nature of the jet disruption changes upon the solidification of the neck.

PRI development is a rather slow process. The minimum jet disruption time for gold is $1/\gamma_{\max} \approx 3\sqrt{\rho R_{\rm j}^3/\sigma} \sim 5$ ns at $\sigma \approx 1000$ dyn cm^{-1}, $R_{\rm j} = 0.05R_{\rm las}$ and $R_{\rm las} = 1$ μm. Neck formation takes a long time, followed by neck narrowing and disruption at an increasing rate. An important point is that, as follows from our MD simulations, the crystallisation zone passes through the neck zone during this time. We deal with disruption near the solid–liquid interface (red-black mark in Fig. 6c; Figs 12, 13). This is the final disruption, in which the last, slowest and coldest, droplet or nanoparticle forms if the frozen material detaches.

It should be emphasised that, after the neck passes through the solidification zone, the neck narrowing mechanism changes fundamentally. In the liquid phase, the increase in narrowing rate is caused by surface tension and the small neck perimeter. Accordingly, the liquid is forced out of the neck by surface tension. In the solid phase, longitudinal neck stretching (along the jet axis) is related to stress concentration per unit surface area in the small cross section of the neck. Stress is then due to the inertia of the material and the residual velocity gradient $\partial w/\partial z$.

Such development of events is typical. Because of this, if the last disruption occurs in the crystalline phase, the closing particle solidifies and the detachment zone on the side of the frozen jet (rod or needle) transforms into an extremely sharp tip. If the last disruption occurs in the liquid part of the jet, a frozen nanodroplet persists on the top of the needle. The corresponding experimental findings are compiled in an excellent paper by Nakata et al. [5].

3.3. Crystallographic structure near the tip

The rod (solidified jet) near the tip is shown in Fig. 14. Atomic coordinates as functions of time were taken from MD simulation. Atoms were imaged using the AtomEye viewer [51]. Figure 14 shows a lateral view of the solidified part of a jet 10 ps after the last jet disruption in the MD simulation. The simulation parameters are indicated in the caption for Fig. 12. The place of neck disruption (tip) is located at the right-hand end of the rod in Fig. 14, which shows the upper part of the jet imaged in Figs 12 and 13. The instant of disruption corresponds to $4.92t_\sigma = 108R_{\rm las}(d_{\rm f}/100)^{1/2}$, where t_σ is in nanoseconds, $R_{\rm las}$ in microns, and $d_{\rm f}$ in nanometres (Fig. 12). The estimate was made for a gold film with $\sigma = 1000$ dyn cm^{-1} and $\rho = 19.3$ g cm^{-3}. In the case represented in Fig. 3 [5], this time is ~53 ns at $R_{\rm las} = 650$ nm and a gold film thickness $d_{\rm f} = 57$ nm. The radius $R_{\rm las}$ in the MD simulation (Figs. 12–14) was a factor of 10 smaller than that in Nakata et al. [5]. At the same time, the velocity $w_{\rm cm}^{\rm br}(0)$ and thermal conductivity in our MD simulations were adjusted so that they corresponded to experimental data in terms of the similarity parameters w_σ

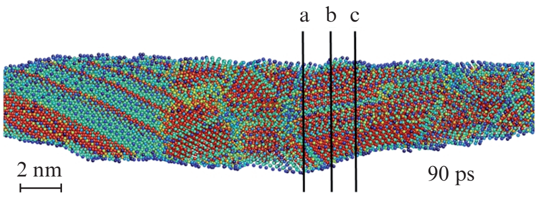

Figure 14. (Colour online) Crystal structure of the solidified jet (lateral view). The last droplet detached 10 ps before the instant represented here. The initial instant, 90 ps, is chosen arbitrarily. The time elapsed since the arrival of an ultrashort laser pulse is the same as in Fig. 12. Red and blue colours correspond to FCC and HCP lattices. The dark blue atoms are located on the surface of the rod (a – c are planes normal to the rod axis).

and w_χ. Nevertheless, the tip radius in MD simulation was a factor of 5 – 6 smaller than that in Nakata et al. [5]. This seems to be due to the higher stretching rate in the neck zone in our MD simulation.

The colour scale in Fig. 14 begins from below, from a dark blue colour, which corresponds to the smallest central symmetry parameter s, to blue, green and yellow in order of increasing s. The highest s value is represented by a red colour. In this MD simulation, the red colour refers to a face-centred cubic (FCC) packing. In the case of a body-centred cubic (BCC) crystal, the parameter s is still larger. We do not detect such packing in our MD simulation. The blue colour corresponds to a hexagonal close-packed (HCP) lattice.

Figure 15 presents two longitudinal axial sections of the rod shown in Fig. 14. The sections are perpendicular to each other and pass through the central part of the rod. The upper section in Fig. 15 passes through a plane parallel to the plane of Fig. 14. Comparing Figs 14 and 15, we can evaluate the depth of the structures visible on the lateral surface. Surprisingly, star-shaped structures persist in the two, mutually perpendicular planes. These structures are located between two structures formed by shear bands. It seems likely that the formation of the shear bands is caused by the tensile stress that acted in the freezing stage. Such bands were detected near the tip of a rod in an experimental study by Nakata et al. [5], but they observed two systems of bands with opposite signs of the angles to the rod axis and there were no bands with an HCP structure.

Figure 16 shows cross sections of the rod along planes a – c (Fig. 14) normal to its axis. One can see a structure, presumably, of icosahedral symmetry, as in Fig. 15. Attention should be paid to the faceting of the cross sections. Similar faceting of a rod produced by a laser pulse was observed in experiments [5].

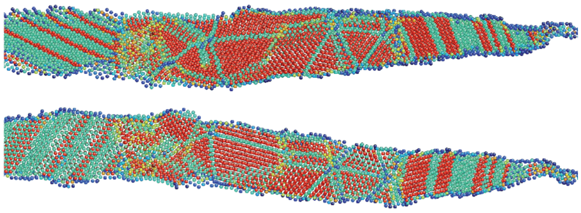

Figure 15. (Colour online) Longitudinal sections of the rod shown in Fig. 14. The sections are perpendicular to each other and the upper section is parallel to the plane of Fig. 14.

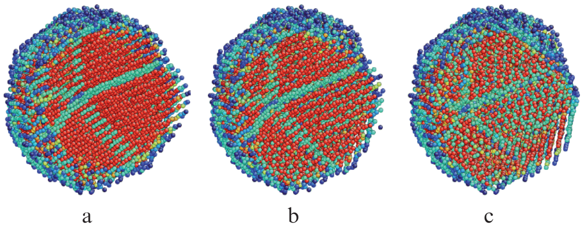

Figure 16. (Colour online) Cross sections of the rod along planes a – c (Fig. 14). Structures with fivefold symmetry and inner sectors filled with an HCP crystal.

Structures of fivefold symmetry were studied in detail by Wu and Zhigilei [52]. They considered the formation and growth of a viable crystalline nucleus in the course of homogeneous nucleation. Their results demonstrate how, in the growth stage, a structure of fivefold symmetry emerges and begins to grow on the edge of an FCC nucleus. This is due to the formation of a twin line. Steinhardt et al. [53] and Frank [54] considered the growth of a crystallite from a nucleus in the shape of an icosahedron in a supercooled homogeneous liquid. According to their results, the energy of an icosahedron in the case of the Lennard-Jones potential is lower than the energy of a 13-atom FCC crystallite. As pointed out by Steinhardt et al. [53], the growth of a crystallite from an icosahedron is energetically hindered, so icosahedra are, so to speak, 'dead-end' nuclei compared to 13-atom nuclei with FCC symmetry.

Figure 17 presents an atomic-scale illustration of the disruption process in the solid phase. Longitudinal stress concentrates in the neck, so the material stretches and the neck becomes thinner and, eventually, ruptures. After disruption, the stretched material contracts and the tip radius decreases. In this process, the tip moves in a complex way, with a considerable transverse component.

The thermal and mechanical dynamics of a detached particle are of great interest. A particle detaches in a mixed state, i.e. it consists of a mixture of a solid and a liquid phase (Figs 12, 13, 17). After detachment, the cooling process ceases, because downward heat transfer along the rod to the dome and film stops. At the same time, the degree of supercooling is so high that the particle gradually becomes completely frozen

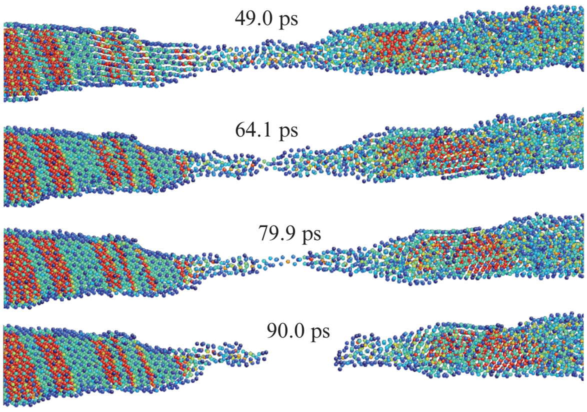

Figure 17. (Colour online) Reduction in neck radius and neck disruption in a solid state (lateral view). The detached nanoparticle is to the right of the disruption point and the forming tip is to the left. The right-hand side was frozen long before the disruption.

in this simulation. For lack of exact axial symmetry, the particle rotates after detachment. Capillarity acts to round off the particle, so it becomes rounded even before complete freezing. Note that, at the beginning of the rounding-off stage, the sharp, solid residue of the neck at the disruption is pulled into the liquid part of the droplet by surface tension.

The parameters of a freezing jet reported by Wu and Zhigilei [52] are similar to those in this study. They performed calculations for silver, a metal similar to gold in a number of characteristics, such as surface tension and thermal conductivity. An important role is played by the cooling rate of a jet because of its small dimensions and high thermal conductivity. As a result, the crystallisation process differs qualitatively from that in a Stefan problem with a continuous temperature variation, a temperature at the solidification front equal to the melting point, and a very slow velocity of the front.

Under our conditions, the liquid phase is highly supercooled (by several hundred degrees Celsius) relative to the melting point. The formation of a homogeneous nucleation zone in front of the solidification interface occurs when the velocity of the interface reaches a limit (70–100 m s^{-1}) imposed by the diffusion rate of atoms in the liquid phase in front of the solidification interface. Under our conditions, the cooling rate, $v_\chi = 100\chi/R_{\rm las}$ (where v_χ is in metres per second, $R_{\rm las}$ in microns and χ in square centimetres per second), exceeds the limiting one, so the effective solidification rate reaches the required value, v_χ, on account of the homogeneous nucleation zone in front of the solidification interface.

In the case of homogeneous nucleation, nuclei of a solid phase spontaneously emerge in the melt due to thermal fluctuations. They are formed in the bulk of the liquid some distance away from the interface. In the case of nucleation on a free surface, a crystallite can build up rows of its atomic planes parallel to the surface of the liquid. Crystalline nuclei forming away from the freezing front are well seen in Fig. 12 and, especially, in Fig. 13, where they are shown on an expanded scale as green dots in a red melt, which are capable of moving upwards, away from the complete solidification region, to a height of ten jet diameters.

External jet formation conditions in this study differ from those in Ref. [52]. Here, a jet is formed because of the capillary deceleration of the flight of a dome (see Section 2). In such a case, the heating spot is small (~1 μm diameter) and the absorbed energy distribution over the spot has a well-defined maximum in its centre. In Ref. [52], a jet, or rather a filament, emerges as a remote consequence of the thermomechanical foaming of a molten metal in a bulk target [11–28, 35, 55–57]. The diameter of the foaming spot on the irradiated surface is large (many microns). Accordingly, there is no well-defined maximum in absorbed energy: displacing the target in its plane by ~1 μm has little effect on the absorbed energy.

In the case of foam, a filament ('jet') results from the breakup of foam membranes [24]. Such membranes restrict vapour bubbles and are flat at a small relative volume of the liquid phase in a two-phase mixture. The structure of foam cells resembles polyhedra or Voronoi mosaics (which are also connected to the names of Descartes, Dirichlet and Delaunay; see Wikipedia). Such structures are encountered as well in crystallography (Wigner–Seitz cells) and cosmology (the large-scale structure of the Universe). Each foam cell consists of membranes (faces), filaments (edges) and vertices (nodes). Each membrane is shared by two neighbouring cells it separates, and each filament is shared by three neighbouring cells. Finally, each vertex, or node, where four filaments meet, is shared by four neighbouring cells.

Cell inflation in foam expanding by inertia is accompanied by a decrease in membrane thickness [24]. Eventually, the membranes rupture one after another and the foam transforms into a network of filaments intersecting in the vertices of polyhedral cells. The filaments link the crater bottom in the residue of the target to the detached dome flying away. In the case of a multitier system of cells, there is a complex network of filaments, because it also consists of several tiers. The tiered structure of laser foam is due to the decrease in the temperature and changes in the initial conditions of nucleation in going from the runaway plate to the bottom of the crater [23–26].

Rapid solidification prevents liquid filaments in the lower tier from completely disappearing in the melt covering the bottom of the crater. The disappearance of the filaments and the residues of the membranes is due to the fact that capillary forces pull the filaments into the melt. Solidification first involves the liquid on the bottom of the crater and then propagates from the base of the filaments along them [22–28, 52]. The upper part of the filaments, close to the runaway dome, breaks up into a droplet fraction, most of which flies away in a vapour droplet plume. At the same time, surface tension brings some of the droplets back to the surface [10, 48]. The droplet fraction is inhomogeneous, because it consists of fragments of the disintegrated membranes and filaments from various tiers, as well as of residues of fragmentation of the runaway dome. Note that the mechanical disintegration and flight of droplets are accompanied by vaporisation and condensation processes, but on the timescale and at the temperatures of interest here these processes have little effect.

Melting, cavitation, foaming, inflation, and collapse of foam have been the subject of extensive studies [5, 11–28, 55–57], which included theoretical analysis [18, 28, 56], MD simulation [18, 28, 56] and experiments [28]. The mechanical characteristics of foam (e.g. its tensile strength) were investigated in Refs [18, 28, 56]. A particularly detailed study was carried out by Mayer P.N and Mayer A.E. [56]. The freezing of nucleation traces in the form of bubbles in a solid matrix was examined in Refs [21–26, 28, 52].

It is worth mentioning two distinctions between filaments in foam and a jet originating from the capillary deceleration of a laser-induced film detachment from the substrate surface. First, the filaments are membrane intersection curves, whereas a capillary jet flies freely. As a rule, three membranes converge to one filament. This influences the shape of the filament and the cooling rate of the filament material. Second, a filament terminates on a runaway shell, whereas a jet has a free top.

There are two scenarios of development: one with a droplet on the top (the last disruption occurs in the liquid phase) and the other with a very sharp tip (the last disruption occurs in the solid phase). The competition between the solidification zone moving upward along the jet and sequential disruptions of the jet has been examined above in detail. In addition, we have analysed the structure of the tip.

4. Conclusions

We have addressed a variety of issues pertaining to 'pointlike' laser irradiation of a thin-film target on a substrate. A focal spot with a diameter of the order of optical wavelengths is here referred to as small. Such spots are produced when a light beam is focused to the diffraction limit. Speaking about 'pointlike' irradiation, we want to emphasise the difference between dynamics in the cases of small and large heating spots on the film surface. At a spot diameter over 10 μm, we failed to obtain a structure in the form of a single dome in our experiments. The present results indicate that the reason for this is that the liquid phase in such a large spot cannot recrystallise before film disintegration.

We have considered the case of weak metallic film adhesion to the substrate, which is of practical importance (for example, for LIFT and nanoplasmonic applications). In a certain range of laser fluences, the film peels off from the substrate as a whole (i.e. without breaking down).

In the case of a laser beam with maximum heating in the centre, the film flying after detachment from the substrate assumes the shape of a dome. We have examined how capillarity leads to the formation and elongation of a liquid jet on the top of the dome. This is caused by the accumulation of the material near the dome axis. Special attention has been paid to the recrystallisation of the melt, of which the dome and jet consist. We have considered the breakup of a liquid jet into liquid droplets as a result of Plateau–Rayleigh instability development.

The crystal structure of a decaying and freezing jet has been studied in detail. We have detected the formation of unusual structures with fivefold symmetry, which correspond to icosahedral atomic order, and analyzed the detachment of the last droplet from the jet, a process that takes place not in a liquid but in a solid state. If the detachment of a liquid droplet leads to a capillary-scale curvature of the top of the dome, detachment in a solid state ends with the formation of a tip with a radius of curvature far below the capillary length scale.

Acknowledgements. This work was supported by the Russian Science Foundation (Grant No. 14-19-01599).

References

1. Korte F., Koch J., Chichkov B.N. *Appl. Phys. A*, **79**, 879 (2004).
2. Unger C., Koch J., Overmeyer L., Chichkov B.N. *Opt. Express*, **20** (22), 24864 (2012).
3. Wortmann D., Koch J., Reininghaus M., Unger C., Hulverscheidt C., Ivanov D., Chichkov B.N. *J. Laser Appl.*, **24**, 042017 (2012).
4. Nakata Y., Okada T., Maeda M. *Jpn. J. Appl. Phys.*, **42**, L1452 (2003).
5. Nakata Y., Miyanaga N., Momoo K., Hiromoto T. *Appl. Surf. Sci.*, **274**, 27 (2013).
6. Nakata Y., Tsuchida K., Miyanaga N., Furusho H. *Appl. Surf. Sci.*, **255**, 9761 (2009).
7. Inogamov N.A., Zhakhovsky V.V., Khokhlov V.A. *J. Exp. Theor. Phys. (JETP)*, **120** (1), 15 (2015) [*Zh. Eksp. Teor. Fiz.*, **147** (1), 20 (2015)].
8. Ivanov D.S., Kuznetsov A.I., Lipp V.P., Rethfeld B., Chichkov B.N., Garcia M.E., Schulz W. *Appl. Phys. A*, **111**, 675 (2013).
9. Ishino M., Faenov A.Ya., Tanaka M., Hasegawa N., Nishikino M., Tamotsu S., Pikuz T.A., Inogamov N.A., Zhakhovsky V.V., Skobelev I.Yu., Fortov V.E., Khokhlov V.A., Shepelev V.V., Ohba T., Kaihori T., Ochi Y., Imazono T., Kawachi T. *J. Appl. Phys.*, **109**, 013504 (2011).
10. Inogamov N.A., Zhakhovsky V.V. *JETP Lett.*, **100** (1), 4 (2014) [*Pis'ma Zh. Eksp. Teor. Fiz.*, **100** (1), 6 (2014)].
11. Starikov S.V., Pisarev V.V. *J. Appl. Phys.*, **117**, 135901 (2015).
12. Zhakhovsky V.V., Nishikhara K., Anisimov S.I., Inogamov N.A. *JETP Lett.*, **71** (4), 167 (2000) [*Pis'ma Zh. Eksp. Teor. Fiz.*, **71** (4), 241 (2000)].
13. Zhigilei L.V., Garrison B.J. *J. Appl. Phys.*, **88** (3), 1281 (2000).
14. Lorazo P., Lewis L.J., Meunier M. *Phys. Rev. B*, **73**, 134108 (2006).
15. Vorobyev A.Ya., Guo Ch. *Opt. Express*, **14** (6), 2164 (2006).
16. Agranat M.B., Anisimov S.I., Ashitkov S.I., Zhakhovskii V.V., Inogamov N.A., Nishihara K., Oparin A.M., Petrov Yu.V., Fortov V.E., Khokhlov V.A. *Appl. Surf. Sci.*, **253** (15), 6276 (2007).
17. Inogamov N.A., Zhakhovsky V.V., Ashitkov S.I., Petrov Yu.P., Agranat M.B., Anisimov S.I., Nishikhara K., Fortov V.E. *J. Exp. Theor. Phys. (JETP)*, **107**, 1 (2008) [*Zh. Eksp. Teor. Fiz.*, **134** (1), 5 (2008)].
18. Zhakhovsky V.V., Inogamov N.A., Nishikhara K. *JETP Lett.*, **87** (8), 423 (2008) [*Pis'ma Zh. Eksp. Teor. Fiz.*, **87** (8), 491 (2008)].
19. Ashitkov S.I., Inogamov N.A., Zhakhovsky V.V., Emirov Yu.N., Agranat M.B., Oleinik I.I., Anisimov S.I., Fortov V.E. *JETP Lett.*, **95** (4), 176 (2012) [*Pis'ma Zh. Eksp. Teor. Fiz.*, **95** (4), 192 (2012)].
20. Gurevich E.L. *Phys. Rev. E*, **83**, 031604 (2011).
21. Wu Ch., Zhigilei L.V. *Appl. Phys. A*, **114**, 11 (2014).
22. Wu Ch., Christensen M.S., Savolainen J.-M., Balling P., Zhigilei L.V. *Phys. Rev. B*, **91**, 035413 (2015).
23. Inogamov N.A., Zhakhovsky V.V., Petrov Yu.V., Khokhlov V.A., Ashitkov S.I., Migdal K.P., Ilnitsky D.K., Emirov Yu.N., Khishchenko K.V., Komarov P.S., Shepelev V.V., Agranat M.B., Anisimov S.I., Oleynik I.I., Fortov V.E. *Proc. SPIE*, **9065**, 906502 (2013); https://doi.org/10.1117/12.2053166.
24. Inogamov N.A., Zhakhovsky V.V., Ashitkov S.I., Emirov Yu.N., Faenov A.Ya., Pikuz T.A., Ishino M., Kando M., Hasegawa N., Nishikino M., Kawachi T., Agranat M.B., Andriash A.V., Kuratov S.E., Oleynik I.I. *J. Phys. Conf. Ser.*, **500**, 112070 (2014).
25. Ashitkov S.I., Komarov P.S., Ovchinnikov A.V., Struleva E.V., Zhakhovsky V.V., Inogamov N.A., Agranat M.B. *Quantum Electron.*, **44** (6), 535 (2014) [*Kvantovaya Elektron.*, **44** (6), 535 (2014)].
26. Inogamov N.A., Zhakhovsky V.V., Khokhlov V.A., Ashitkov S.I., Emirov Yu.N., Khichshenko K.V., Faenov A.Ya., Pikuz T.A., Ishino M., Kando M., Hasegawa N., Nishikino M., Komarov P.S., Demaske B.J., Agranat M.B., Anisimov S.I., Kawachi T., Oleynik I.I. *J. Phys. Conf. Ser.*, **510**, 012041 (2014).
27. Inogamov N.A., Zhakhovsky V.V., Ashitkov S.I., Emirov Yu.N., Faenov A.Ya., Petrov Yu.V., Khokhlov V.A., Ishino M., Demaske B.J., Tanaka M., Hasegawa N., Nishikino M., Tamotsu S., Pikuz T.A., Skobelev I.Y., Ohba T., Kaihori T., Ochi Y., Imazono T., Fukuda Y., Kando M., Kato Y., Kawachi T., Anisimov S.I., Agranat M.B., Oleynik I.I., Fortov V.E. *Eng. Failure Analysis*, **47**, 328 (2015).
28. Ashitkov S.I., Romashevskii S.A., Komarov P.S., Burmistrov A.A., Zhakhovsky V.V., Inogamov N.A., Agranat M.B. *Quantum Electron.*, **45** (6), 547 (2015) [*Kvantovaya Elektron.*, **45** (6), 547 (2015)].
29. Ionin A.A., Kudryashov S.I., Makarov S.V., Seleznev L.V., Sinitsyn D.V., Golosov E.V., Golosova O.A., Kolobov Y.R., Ligachev A.E. *Appl. Phys. A*, **107** (2), 301 (2012).
30. Ionin A.A., Kudryashov S.I., Makarov S.V., Seleznev L.V., Sinitsyn D.V., Ligachev A.E., Golosov E.V., Kolobov Y.R. *Laser Phys. Lett.*, **10**, 056004 (2013).
31. Hashida M., Ikuta Y., Miyasaka Y., Tokita S., Sakabe S. *Appl. Phys. Lett.*, **102**, 174106 (2013).
32. Ionin A.A., Kudryashov S.I., Makarov S.V., Rudenko A.A., Seleznev S.V., Sinitsyn D.V., Kaminskaya T.P., Popov V.V. *JETP Lett.*, **101** (5), 350 (2015) [*Pis'ma Zh. Eksp. Teor. Fiz.*, **101** (5), 382 (2015)].
33. Varlamova O., Reif J., Varlamov S., Bestehorn M., in *Progress in Nonlinear Nano-Optics*. Ed. by S.Sakabe, C.Lienau, R.Grunwald (Springer Int. Publ., 2015) Ch. 1.
34. Zayarnyi D.A., Ionin A.A., Kudryashov S.I., Makarov S.V., Rudenko A.A., Bezhanov S.G., Uryupin S.A., Kanavin A.P., Emel'yanov V.I., Alferov S.V., Khonina S.N., Karpeev S.V., Kuchmizhak A.A., Vitrik O.B., Kul'chin Yu.N. *JETP Lett.*, **101** (6), 394 (2015) [*Pis'ma Zh. Eksp. Teor. Fiz.*, **101** (6), 428 (2015)].
35. Zhakhovskii V., Inogamov N., Nishihara K. *J. Phys. Conf. Ser.*, **112**, 042080 (2008).

36. Rapp L., Haberl B., Bradby J., Gamaly E., Williams J., Rode A., in *Fundamentals of Laser-Assisted Micro- and Nanotechnologies* (Berlin: Springer Intern. Publl. AG, 2014) pp 3–26.
37. Kuchmizhak A., Vitrik O., Kulchin Yu., Storozhenko D., Mayor A., Mirochnik A., Makarov S., Milichko V., Kudryashov S., Zhakhovsky V., Inogamov N. *Nanoscale*, **8**, 12352 (2016).
38. Veiko V.P., Kaidanov A.I., Kovachki Kh.A., Shakhno E.A. *Izv. Ross. Akad. Nauk, Ser. Fiz.*, **56** (4), 169 (1992).
39. Veiko V.P., Shakhno E.A., Smirnov V.N., Miaskovski A.M., Nikishin G.D. *Laser Part. Beams*, **24**, 203 (2006).
40. Emel'yanov V.I., Zayarnyi D.A., Ionin A.A., Kiseleva I.V., Kudryashov S.I., Makarov S.V., Nguyen C.T.H., Rudenko A.A. *JETP Lett.*, **99** (9), 518 (2014) [*Pis'ma Zh. Eksp. Teor. Fiz.*, **99** (9), 601 (2014)].
41. Inogamov N., Zhakhovskii V., Ashitkov S., Khokhlov V., Shepelev V., Komarov P., Ovchinnikov A., Sitnikov D., Petrov Yu., Agranat M., Anisimov S., Fortov V. *Contrib. Plasma Phys.*, **51** (4), 367 (2011).
42. Anisimov S.I., Kapeliovich B.L., Perel'man T.L. *Sov. Phys. JETP*, **39** (2), 375 (1974) [*Zh. Eksp. Teor. Fiz.*, **66** (2), 776 (1974)].
43. Petrov Yu.V., Inogamov N.A., Migdal K.P. *JETP Lett.*, **97** (1), 20 (2013) [*Pis'ma Zh. Eksp. Teor. Fiz.*, **97** (1), 24 (2013)].
44. Migdal K., Petrov Yu., Inogamov N. *Proc. SPIE*, **9065**, 906503 (2013); https://doi.org/10.1117/12.2053172.
45. Petrov Yu., Inogamov N., Anisimov S., Migdal K., Khokhlov V., Khishchenko K. *J. Phys.: Conf. Ser.*, **653**, 012087 (2015).
46. Migdal K., Petrov Yu., Il'nitsky D., Zhakhovsky V., Inogamov N., Khishchenko K., Knyazev D., Levashov P. *Appl. Phys. A*, **122**, 408 (2016).
47. Petrov Yu., Migdal K., Inogamov N., Zhakhovsky V. *Appl. Phys. B*, **119**, 401 (2015).
48. Inogamov N., Zhakhovsky V., Migdal K. *Appl. Phys. A*, **122**, 432 (2016).
49. Kuznetsov A.I., Koch J., Chichkov B.N. *Appl. Phys. A*, **94**, 221 (2009).
50. Kul'chin Yu.N., Vitrik O.B., Kuchmizhak A.A., Savchuk A.G., Nepomnyashchii A.A., Danilov P.A., Zayarnyi D.A., Ionin A.A., Kudryashov S.I., Makarov S.V., Rudenko A.A., Yurovskikh V.I., Samokhin A.A. *J. Exp. Theor. Phys. (JETP)*, **119** (1), 15 (2014) [*Zh. Eksp. Teor. Fiz.*, **146** (1), 21 (2014)].
51. Li J. *Modelling Simul. Mater. Sci. Eng.*, **11**, 173 (2003).
52. Wu Ch., Zhigilei L.V. *J. Phys. Chem. C*, **120**, 4438 (2016).
53. Steinhardt P.J., Nelson D.R., Ronchetti M. *Phys. Rev. B*, **28**, 784 (1983).
54. Frank F.C. *Proc. R. Soc. London Ser. A*, **215**, 43 (1952).
55. Norman G.E., Starikov S.V., Stegailov V.V., Saitov I.M., Zhilyaev P.A. *Contrib. Plasma Phys.*, **53** (2), 129 (2013).
56. Mayer P.N., Mayer A.E. *J. Appl. Phys.*, **120**, 075901 (2016).
57. Pohl R., Visser C.W., Roemer G.-W., Lohse D., Sun Ch., Veld B.H. *Phys. Rev. Appl.*, **1**, 024001 (2015).